Research Square

Preprints are preliminary reports that have not undergone peer review.
They should not be considered conclusive, used to inform clinical practice,
or referenced by the media as validated information.

Impact of Particle Roughness on Packing

Adrien Luyckx

Adrien.Luyckx@uliege.be

University of Liège

Eric Opsomer

University of Liège

Research Article

Keywords: Simulation, Non convex, Packing, Roughness

Posted Date: April 9th, 2026

DOI: https://doi.org/10.21203/rs.3.rs-9354781/v1

License: This work is licensed under a Creative Commons Attribution 4.0 International License.
Read Full License

Additional Declarations: No competing interests reported.

Impact of Particle Roughness on Packing

Adrien Luyckx[1*] and Eric Opsomer[1]

[1]Physics Department, GRASP Institute, Liège, 4000, Belgium.

*Corresponding author(s). E-mail(s): Adrien.Luyckx@uliege.be;
Contributing authors: Eric.Opsomer@uliege.be;

Abstract

The quest to the control packing fraction has a long pedigree, from early insights into dense sphere packings and their modern proofs to contemporary efforts that extend beyond spheres to frictional, anisotropic, and non convex grains. However, a unifying picture that ties particle roughness across scales to macroscopic packing remains incomplete. We address this gap via Discrete Element Method simulations with a multi sphere representation to quantify particle roughness at three scales: microscopic (surface friction), mesoscopic (furrow depth set by the number of spheres used to approximate a rod), and macroscopic (overall shape: rod, cross and star). After gravity deposition, we measure the pile height, packing fraction, coordination number, and force networks. The results clearly show scale separation. Reducing mesoscopic roughness promotes sliding and compaction, reducing pile height following a linear trend while leaving the coordination numbers and force distributions essentially unchanged. In contrast, macroscopic roughness controls pile architecture: progressing from rods to crosses to stars increases the pile height and alters the coordination numbers and the tails of force distributions. We propose a compact semi empirical framework that links the packing fraction to the three roughness scales.

Keywords: Simulation, Non convex, Packing, Roughness

1 Introduction

One ancient but still unresolved question is how objects are arranged optimally in space and fill a given volume leading to different packing fractions. In particular philosopher and scientist have focused specifically on how granular material properties can impact those arrangements [1]. This specific interest in granular materials arise from several applications. In agri-food, where researcher study discharge of hopper to manage correctly their behaviour [2–4]. In pharmaceutical industries, where the rheological properties of the particles are of great interest to understand how active constituent can be delivered in the desired zone [2, 4]. In concrete industries, where mechanical and mixing properties can be studied in depth to understand how the right properties arise [2, 5].

To understand the packing of granular assemblies, researcher first studied the mono disperse packing of spheres because of its simplicity. Thomas Harriot, on the demand of Sir Walter Raleigh, was the first to address this problem to arrange cannonball optimally [6]. Later, Johannes Kepler discovered that Face-Centered Cubic (FCC) achieve 74% packing efficiency, with each ball touching 12 neighbours without being able to prove mathematically that this was highest achievable value [1]. A formal proof was only accepted in 2017 [7] taking the advantage of the

work of Kepler and Gauss while also capitalizing on new computational power and confirming what was known for a long time, the closest packing of spheres has a packing fraction of $\phi_{\text{FCC}} = \frac{\pi}{3\sqrt{2}} \approx 0.74$ [1]. In addition, a similar but more complex problem is the polydisperse case, studied by Apollonius of Perga and Descartes and led to only semi analytical solution such has the Furnas model [1, 8–10]. However, life is not always optimal, if one pours granular materials in a container, a sub optimal solution is obtained, also known as Random Loose Packing (RLP) with $\phi_{\text{RLP}} = \frac{1}{1+\sqrt{3}/2} \approx 0.54$ and when vibrated or compressed, tends towards a denser solution, Random Close Packing (RCP) with $\phi_{\text{RCP}} = \frac{1}{1+\sqrt{3}/3} \approx 0.63$ [11]. Most of the time, the results in this field remain empirical, even though pioneering work led by Edwards on the statistical mechanics of granular matter has formalized the field, helping, for example to understand the relationships among the packing fraction, coordination number and coefficient of friction [11–13].

In industry, shapes are different than spheres. In a concrete matrix, apart from their polydisperse nature, the shape of aggregates are far rougher than those of spheres. This roughness makes understanding and modelling more complex, but through experiments and simulations, important differences have been observed between convex and non convex shapes where toy-model shape such as spherocylinders polypods or star-shaped objects have been used [14–17]. For example, Aponte *et al.* have shown that the stability of piles without any containers can be obtained with the introduction of non convexity where the shape acts like a keystone [18]. Moreover, frictional roughness, which comes from the microscopic scales of the surface [19–23], impacts the mechanical behaviour of piles, such as the packing fraction, coordination number, force distributions and flow [11, 24–31]. Instead of modelling shapes explicitly in simulations, a range of methods have been developed to model geometric effects through a rolling resistance added to the usual friction coefficient [32–34]. This method is not easily interpretable and leads to some misuse which tends to introduce undesirable macro properties such as change in the elastic modulus and Poisson's ratio of the granular assembly [35, 36].

During the last decades, research has focused on how particle shape (macrsocopic roughness) or interparticle friction (microscopic roughness) can change the packing properties, in particular the packing fraction, of a granular pile [11, 37]. In this article, we study these properties while changing rugosity at a less explored mesoscopic level which is characterized by the bumpyness of a particle's surface (see Figure 1b). We fix the microscopic roughness and realize a Discrete Element Method (DEM) simulations of granular packings made of three different shapes (rod, cross, star) and vary the mesocopic rugosity by modifying the sphere-based volume representation of our particles. Our approach allows us to develop and validate a semi-empirical model linking the pile's packing fraction to the different rugosity levels.

2 Methods

In this section, we describe our particles and the main characteristics of our in-house code [38]. The usual roughness lies at the microscopic level;

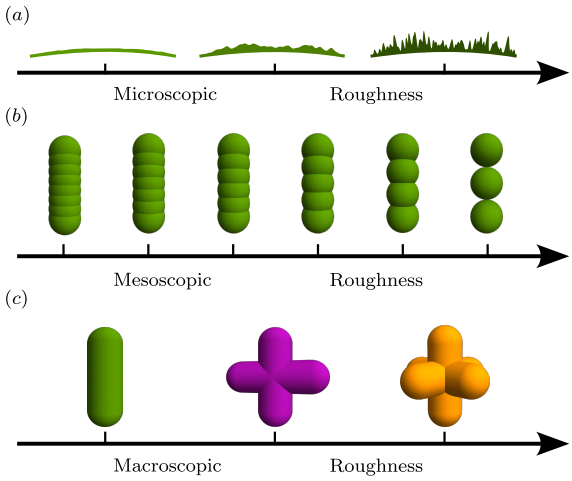


Fig. 1 (*a*) Sketch of the microscopic roughness on the surface of a sphere. (*b*) Visualization of the mesoscopic roughness for the rods with 8,7,6,5,4, and 3 spheres in their description. (*c*) Visualization of the macroscopic roughness for the rod (green), cross (orange) and star (purple) with 32 spheres in the description of their rods.

known as the coefficient of friction of a material onto another material, we keep this roughness fixed at 0.4, named later microscopic roughness. We sketch this roughness in Figure 1a. Part of this microscopic friction arises from asperities on

the surface of objects, and a small microscopic roughness will arises from flat surfaces, whereas a greater microscopic roughness arises from rougher surfaces. Depending on the shape, particles will have different contacts; and thus, we treat the shape as a level of macroscopic roughness. We study three shapes, Rod, Cross and Star, from which a level of macroscopic roughness arises. Each of the three shapes are composed of 1, 2 and 3 rods, which are orthogonal to one another (see Figure 1c). A way to model those shapes is the *multi spheres* approach [39, 40], which represents objects through the aggregation of spheres that might overlap. In fact, our intermediate level of roughness, the mesoscopic level, depends on how many spheres will compose each object if the spheres are uniformly distributed in the rods. A good way to understand this is through the furrow height f_n where n is the number of spheres in our description. Any change in this height leads to a change in our mesoscopic roughness. In Figure 2, we present a visualization of the rod length L, the sphere radius R and the furrow height f_n. This furrow height is measured from the axis of revolution of the rod to the intersection of two spheres, and it can be proven that,

$$f_n = \sqrt{1 - \left(\frac{2}{n-1}\right)^2} R, \tag{1}$$

we choose to vary n in the range $[3, 12]$ adding also 32 as an asymptotic value. Similar to the microscopic roughness, the coefficient of friction is used, we propose a parameter for the mesoscopic one, μ_{meso}. For a flat surface, we have $f_n = R$, whereas we tend to expect it to be attached with a mesoscopic roughness of 0 because two smooth rods might easily slide on each other and in contrast, one with $f_n = 0$ to $\mu_{\text{meso}} = 1$. A finer visualization is shown in Figure 1b. Thus, we introduce,

$$\mu_{\text{meso}} = 1 - \frac{f_n}{R}. \tag{2}$$

Note, that we often use micro, meso and macro-roughness to shorten microscopic, mesoscopic and macroscopic roughness.

To understand the impact on the different roughnesses, we choose to fix the mass m and inertia tensor I to that of the smooth object

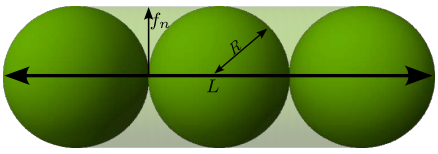


Fig. 2 Visualization of the length of a rod, radius of a sphere and deepest furrow. We show one rod with 3 spheres and one with increased transparency with 32 spheres.

with $n \to \infty$. These values are obtained analytically, while the volume of each particle can be computed through 3D voxelization which slices spaces in small voxels of size $10^{-6}R$. More details on our particle description can be found in the Appendix A. Additionally, the number of particles N is chosen so that the total mass in each pile is conserved.

Simulations are based on DEM [41–43], which originated in the pioneering work of Cundall and Strack [44]. While several space-time integration schemes exist [45–48], we choose to select the new angular orientation integration SPIRAL [46] for its balance between accuracy and computational time for shapes more complex than spheres and use with a classic leapfrog for positions that are based on the usual rigid body dynamics with equations,

$$\mathbf{F} = m\mathbf{a} \qquad \mathbf{I}\dot{\boldsymbol{\omega}} + \boldsymbol{\omega} \times (\mathbf{I}\boldsymbol{\omega}) = \boldsymbol{M}.$$

DEM also depends on the choice of contact model [49], and we choose to take the most common model, the Hertz-Mindlin model with normal and tangential forces, F_n and F_t, which has the form,

$$F_n = K_n \delta_n^{3/2} + \eta_n v_n \qquad F_t = K_t \delta_t^{3/2} + \eta_t v_t.$$

where δ_n prevents the particles from entering into another, and δ_t maintains them in contact when forces push them to slide on one another. A part from that, the term in ηv acts as a damping term pushes the contact to reach equilibrium. The last force acting on our particles that drives the dynamics is gravity, $m\mathbf{g}$, which acts in the vertical direction.

We present in Table 1 the parameter of our simulations. For more detail on DEM simulation, see, for example [41] and the Appendix B and C.

Finally, to extract statistical data, we performed random seed-based deposition for the particles with 100 different seeds for each pair of

Table 1 Simulation parameters

Property	Ranges of values
Density, ρ	$1.2 \times 10^3\,\mathrm{kg\,m^{-3}}$
Young's Modulus, E	$2.5 \times 10^9\,\mathrm{Pa}$
Poisson's Ratio, ν	0.35
Coefficient of Restitution, e	0.3
Coefficient of Friction, μ	0.4
Box Dimension, $l_x \times l_y \times l_z$	$0.1 \times 0.1 \times 0.5\ \mathrm{m^3}$
Maximum Simulation Time, t_{max}	15 s
Time Step, dt	$1 \times 10^{-6}\,\mathrm{s}$
Shapes	Rod,Cross,Star
Number of Particles, N	3780,2268,1620
Mass, $m_{\mathrm{rod}}, m_{\mathrm{cross}}, m_{\mathrm{star}}$	0.3139,0.5277,0.7301 g
Moment of inertia along x, I_{xx}	5.2, 5.8, 10.7 $\mu\mathrm{g\,m^2}$
Moment of inertia along y, I_{yy}	5.2, 10.1, 10.7 $\mu\mathrm{g\,m^2}$
Moment of inertia along z, I_{zz}	5.2, 5.8, 10.7 $\mu\mathrm{g\,m^2}$
Sphere radius, R	$2.5 \times 10^{-3}\,\mathrm{m}$
Rod Length, L	$6R$
Gravity, g	$9.81\,\mathrm{m\,s^{-2}}$

(macro, meso) roughness, we thus have $3 \times 11 \times 100 = 3300$ simulations.

3 Results

In this section we present how common observables such as the pile height H, packing fraction ϕ, coordination number Z and force distribution vary with meso and macro-roughness at the last frame of our simulations. Each observation will be put into perspective from what is known for the microscopic roughness from the literature.

3.1 Pile Height

As a starting point, let us focus on Figure 3 where 6 representative piles have been extracted from our data, two for each macro roughness with $\mu_{\mathrm{meso}} = 1$ and approximately 10^{-1}. We see that the pile height normalized by the size of a Rod L can vary significantly with μ_{meso} and macro roughness. Going from Rod to Cross then Star, we see a clear increase in pile height explained easily by the fact that Star has fewer degrees of freedom than Cross does and is thus stuck in a looser packing. While increasing μ_{meso} tends to decrease the pile height with an effect modulated by the shape, rods have larger differences than crosses which are greater than those of stars. This trend is again guided by the degrees of freedom because we remove volume inside each rod by carving their furrows, thus reducing the pile height.

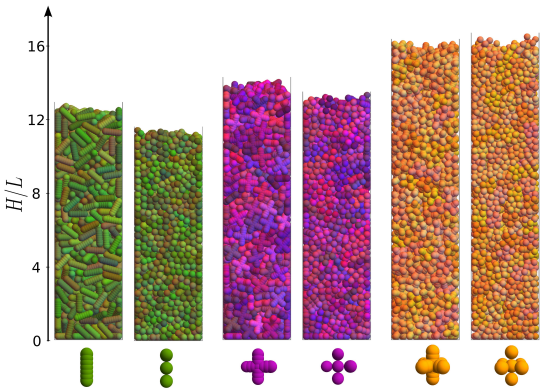


Fig. 3 Visualization of Rod (green), Cross (purple) and Star (orange) with each $\mu_{\mathrm{meso}} = 1$ and approximately 10^{-1} from left to right. The axis represents the height H of the pile normalized by the rod length, H/L.

Now that we have seen the typical configuration that occurs, let us present all our data for the pile height normalized by the length of a Rod L. Figure 4a shows the evolution of H_{max}/L with the meso roughness. Colour variations represent different values of macro roughness and solid lines correspond to equation (3). In general, with increasing micro roughness, we expect the height to increase because surfaces can hardly slide on one another [11]. The opposite trend is observed with meso roughness and represented with a linear model, such that,

$$H_{max}(n) = H_1 + H_\Delta(1 - \mu_{\mathrm{meso}}). \qquad (3)$$

Here, H_1 is associated with the minimal height observed, when $\mu_{\mathrm{meso}} = 1$, and H_Δ is associated with the variation due to the change in meso-scale roughness. An interesting phenomenon occurs for the highest macro roughness, the Star, where the normalized height does not vary much in comparison with the Rod and Cross heights, confirming the observation in Figure 3. This can be explained by the fact that Star, in contrast to Rod and Cross cannot interlock because their degrees of freedom are reduced by their extent in the three directions of space. Finally, in contrast to the first two roughnesses, the macro roughness tends to increase the

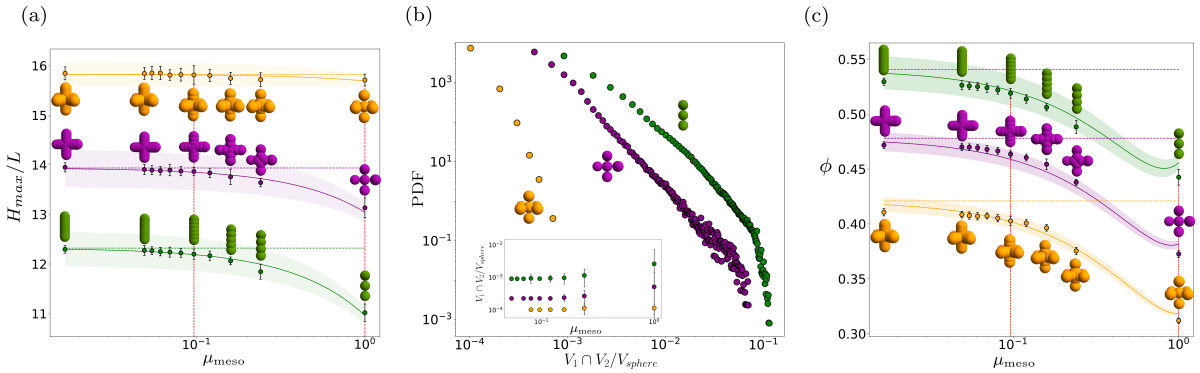


Fig. 4 Average and standard deviation result of 100 simulations for Rods (green), Crosses (purple) and Stars (orange). The solid lines represent our models, and the coloured region represents one standard deviation of our model. Finally, the dashed lines are guides for the eye; red lines are related to the μ_{meso} of the pile shown in Figure 3 and the other line are related to the extrapolated values of our models when $\mu_{\text{meso}} = 0$. The reader is referred to the text for a detailed analysis. **(a)** Evolution of the maximum height normalized by the rod length, H_{max}/L, with the meso-scale roughness μ_{meso}. The log scale allows us to distinguish values close to zero better. The model here is associated with equation (3). **(b)** Probability Density Function (PDF) of the overlap between the convex-hulls of particles normalized by the volume of a sphere for Rods, Crosses and Stars with $\mu_{\text{meso}} = 1$. In the inset, the evolution of the same shape overlaps with the meso-roughness μ_{meso}. Here, the error bars represent the minimum and maximum values observed in the distributions and we keep the mean because the median was always equal to zero. **(c)** Evolution of the packing fraction ϕ with meso-roughness (μ_{meso}). The log scale allows us to distinguish values close to zero better. Model here is associated with equation (6).

pile height due to the increase in the number of arms of each shape. These observations push us to interpret $1 - \frac{H_\Delta}{H_1}$ as a measure of macro roughness μ_{macro} which matches our expectation that stars are rougher than crosses which are rougher than rods. We have here for Rod, Cross and Star, $\mu_{\text{macro}} \approx \{0.88, 0.94, 0.99\}$

3.2 Convex-hull overlap

To complement this analysis and support our point that interlocking is at the heart of the normalized height reduction, we introduce the normalized overlap between the convex-hulls of particles that are in contact. The idea behind this measure is to take the convex-hull around each rod being part of a particle to make a single hull for a given particle and then take the intersection between the pairs of hulls obtained, which is finally normalized by the volume of a sphere for simplicity, a clear visualisation of that can be seen in Figure 5.

Due to the fact that DEM treat contact through overlap, we had to take a given cut-off on our values. Typically, particles in contact always overlap up to a given level. In our case, we can evaluate this value when we compare normal contact forces with gravity, where at equilibrium, $F_n = mg$. We take m as $16m_{\text{star}}$ because in our system particles in the bottom of our pile can feel all the weight of the particles above them, because Janssen effect is not significant as our pile is narrow and particles are far from spherical [50–53]. To have an upper bound, we thus take about 16 star masses as one can be observed in Figure 3. Afterwards, using numerical parameters given in Table 1 and Appendix C informations about our contact model, we then obtain, assuming that the

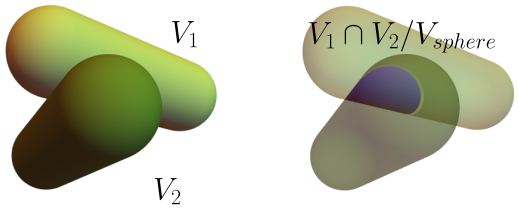


Fig. 5 Visualisation of our convex-hull measure taken from our simulation data. On the left, each green rods were made of 3 spheres and we took the convex-hull round each of them having volume V_1 and V_2. On the right, we depict the intersection in blue between these two volumes and underline the fact that our measure is normalised with the volume of a spheres.

normal velocity $v_n \approx 0$,

$$\hat{\delta}_n = \left(\frac{16 m_{\text{star}} g}{K_n}\right)^{\frac{2}{3}} \approx 5.10^{-4} R \tag{4}$$

where K_n is the normal spring stiffness in the Hertzian model. Taking a factor 10 for safety on our bound, and noticing that overlap of sphere are basically related to spherical cap volume, we can estimate the value of our lower bound bound volume normalized by the volume of a sphere through $10\hat{\delta}_n^2 R/R^3 \approx 10^{-6}$.

Removing all data under this lower bound we can thus interpret this as a measure of interlocking between particles and present in Figure 4b, the Probability Density Function (PDF) for our three macro roughnesses with $\mu_{\text{meso}} = 1$ because their empty furrows should provide more interlocking, We can see that indeed rods and crosses have greater overlap than stars do, supporting the idea that an increase in the normalized height comes from interlocking. In addition, the inset shows the general trend observed for our three macro roughnesses with varying meso roughness.

3.3 Packing fraction

With this in mind, we can now focus on the packing fraction ϕ, which is a usual quantity studied to characterise the packing of different shapes. This quantity is simply the ratio between the occupied volume of the particles divided by the overall volume they are enclosed in. In our case of a mono-dispersed granular column made with different shapes, it is thus proportional to the number of individual shapes and their volume Nv_n and inversely proportional to the volume of the heap approximated here with a fixed basis of size $l_x \times l_y$ and a height H_{max}, which explains the first line in equation (6). In Figure 4c, we present its evolution against the meso-roughness μ_{meso} and with the change in colour related to each macro-roughness. With increasing microscopic roughness, a decrease in the packing fraction is usually observed because the pile height increases as shape is restrained by friction. In the case of meso-roughness, something else happens, one contribution comes from the fact that the volume of particles decreases with μ_{meso} because furrows are being carved, resulting in a decrease in the packing fraction. The other contribution comes from the change observed in the height, which is observable only for values close to $\mu_{\text{meso}} = 1$. Finally, with macro roughness, the packing fraction tends to decrease because the pile height decreases as explained before. In order to understand all these changes, let us approximate the volume of the heap by $V_{max} = l_x l_y H_{max}$ and express the volume of the particles v_n as a function of μ_{meso},

$$v_n = \frac{(1-\mu_{\text{meso}})^2 + 3}{4} v_\infty, \tag{5}$$

see Appendix A for more details. We can then model the packing fraction through,

$$\begin{aligned}
\phi(\mu_{\text{meso}}, \mu_{\text{macro}}) &\approx \frac{N v_n}{V_{max}} = \frac{N}{l_x l_y} \frac{v_n}{H_{max}} && (6)\\
&= \frac{N v_\infty}{4 l_x l_y} \frac{(1-\mu_{\text{meso}})^2 + 3}{H_\Delta (1-\mu_{\text{meso}}) + H_1} && (7)\\
&= \phi_1 \frac{(1-\mu_{\text{meso}})^2 + 3}{3(1-\mu_{\text{macro}})(1-\mu_{\text{meso}}) + 3}. && (8)
\end{aligned}$$

where $\phi_1 = \frac{3 N v_\infty}{4 l_x l_y H_1}$ is simply an estimation of the packing fraction for $\mu_{\text{meso}} = 1$ and v_n is the volume of a particle with n spheres approximated here to the one of a Rod. We use the relation $\mu_{\text{macro}} = 1 - \frac{H_\Delta}{H_1}$ introduced in the height analysis for clearer interpretation. In our case, we obtain $\phi_1 = \{0.45, 0.39, 0.33\}$ for Rod, Cross and Star. Please note, that although microscopic friction μ is not present directly in the equation, other studies have shown its impact on the packing fraction [11, 24–30].

Looking at the curves related to equation (8) in Figure 4c, we see a minimum in the packing fraction. Its appearance can be explained by the competition between the quadratic decrease in particle volume v_n and the linear decrease in pile height H_{max}. As μ_{macro} is increasing, this minimum is shifting to higher values of μ_{meso}, whose expression is given by,

$$\hat{\mu}_{\text{meso}} = \frac{2 - \mu_{\text{macro}} - \sqrt{1 + 3(1-\mu_{\text{macro}})^2}}{1 - \mu_{\text{macro}}} \tag{9}$$

assuming $(\mu_{\text{meso}}, \mu_{\text{macro}}) \in [0,1] \times [0,1]$. Studying the simplest case, where $\mu_{\text{macro}} \to 1$, such that $H_\Delta \to 0$ as for Star, we get that $\hat{\mu}_{\text{meso}} \to 1$. Another aspect that could be interesting to study

from this perspective is the different extremum in packing fractions.

Finally, it is to note that ϕ has a pre-factor ϕ_1 scaling the final value and decreases with the macro-roughness. Even though more shapes would be needed to characterise this evolution and make conclusions, we expect the prefactor ϕ_1 to evolve within $[0.1 - 0.8]$ from the usual values measured for the RLP going from elongated rods to tetrahedral shapes [54, 55]. Our function creates variation in the range $[10 - 30]\%$, which thus remains significant in the case of packing fraction values.

3.4 Coordination number

During our study, we noted that particles could interlock, which encouraged us to study the coordination number Z and the distribution of forces related to interlocking. In Figure 6, we present the coordination number for all our mesoscopic and macroscopic roughnesses. Usually, an increase in the microscopic roughness is known to reduce the coordination number because for higher values, movement is restrained and leads to a lower packing with less contact [11]. In contrast, with our meso-roughness, coordination remains constant and thus does not follow packing fraction evolution. With increasing macro-roughness, the coordination number tends to decrease following the behaviour of the packing fraction.

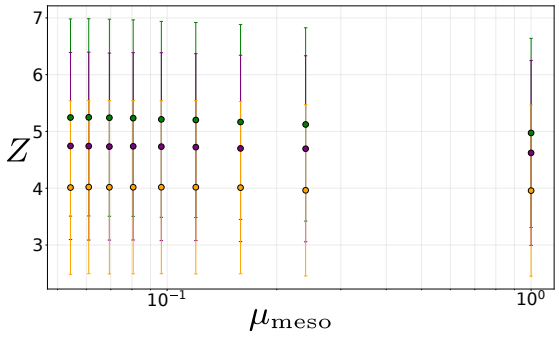


Fig. 6 Mean coordination number Z along with its standard deviation as a function of the meso-roughness μ_{meso}. The log scale allows us to distinguish values close to zero better. Data represent our mean and standard deviation over our 100 simulations where Rod, Cross and Star associated with green, purple and orange.

3.5 Forces distribution

In addition, in Figure 7, we present the force distributions when $\mu_{\mathrm{meso}} = 1$, removing values associated with particles in contact with walls to avoid boundary effects. A usual way to study this distribution is through an exponential fit of the form $A \exp\left(-\beta \tilde{F}\right)$ for $\tilde{F} > 1$, with A being the amplitude, β is the decay rate and $\tilde{F} = \frac{F}{\bar{F}}$ where $\bar{F}$ is the mean force observed in a pile and F is the studied force [56–58]. In our case, we focused on

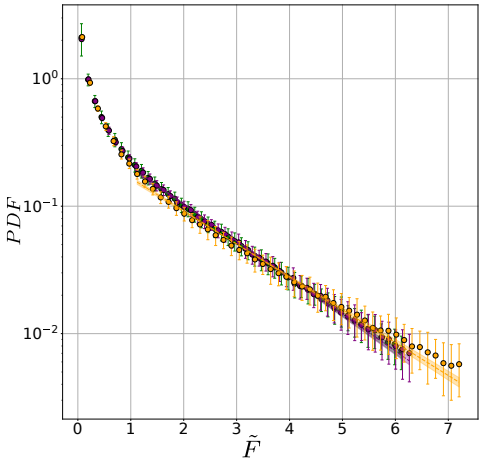


Fig. 7 Probability distribution of the mean observed forces $\tilde{F}$ along the normal direction of the contacts. Data represents our mean and standard deviation over our 100 simulations with $\mu_{\mathrm{meso}} = 1$, where Rod, Cross and Star are associated with green, purple and orange, respectively.

normal and tangential forces, and we report the amplitude and decay rates in Figure 8 for all our meso and macro roughness conditions in the case of normal forces because tangential forces have the same behaviour and amplitudes, as shown in the Appendix D. Usually, this distribution does not change with microscopic friction but tends to be impacted by the deformation of particles [59]. Indeed, in our case, mesoscopic roughness does not significantly affect the values of our fitting parameters, whereas macroscopic roughness tends to decrease them. This is comprehensible given the fact that the region influenced by a particle is changed and thus deformed in a sense when we transform a rod in a cross, for example. Moreover, others studies have shown that particle's shape impact strongly forces distribution leading to a power law scaling for $\tilde{F} < 1$ due to rearrangement

of the force network [60, 61], this is what we also observe.

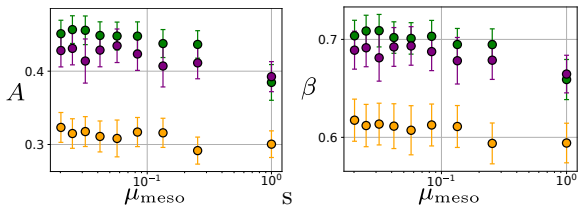


Fig. 8 Amplitude and decay rate of the exponential fit for the observed normal forces where $\tilde{F} > 1$ along with its standard deviation as a function of the meso-roughness μ_{meso}. The log scale allows to distinguish values close to zero better. The data represent our mean and standard deviation over our 100 simulations where Rod, Cross and Star are associated with green, purple and orange, respectively.

usually do not vary with microscopic roughness. In our case, mesoscopic roughness had no impact, whereas macroscopic roughness did, making sense, as previous study noted that important particle deformation was needed to change it [59].

Table 2 Different kind of roughness presented in this paper. Symbolic dependence of μ with the microscopical scale of the the surfaces is shown via σ and explicit dependence of the mesoscopic and macroscopic roughness respectively through f_n the furrow depth w.r.t R the radius and H_Δ the variation in height w.r.t. H_1 the height of pile with $\mu_{\text{meso}} = 1$.

Roughness	**Expression**
Microscopic	$\mu(\sigma)$
Mesoscopic	$\mu_{\text{meso}} = 1 - \frac{f_n}{R}$ (2)
Macroscopic	$\mu_{\text{macro}} = 1 - \frac{H_\Delta}{H_1}$ (3)

4 Conclusion & Perspectives

In this paper, we introduce two new concepts, mesoscopic and macroscopic roughness. The key idea is to start from the well-known microscopic roughness, also known as the friction coefficient, and then extend this idea to higher level of the particles. The mesoscopic roughness corresponds to an intermediate scale characterized by the depth of the furrow along the surface of the particles and the macroscopic roughness to the impact on the pile height from the overall shape of the particles, where mathematical expressions are summarized in Table 2. These new terms help us to compare easily several common observables, such as the height of piles, packing fraction, coordination numbers and force networks. Moreover, we were able to introduce a semi empirical model for the packing fraction that represents our data well with the justification that it should be dependent on the three scales of roughness. In contrast to the usual microscopic roughness, our mesoscopic roughness does not impact the coordination number, whereas the macroscopic roughness does. This allows us to understand the phase diagram of granular matter introduced in the Edwards theory [11] differently, when the coordination number is a function of the packing fraction, we see that for a fixed macroscopic roughness, the mesoscopic roughness draws horizontal lines with constant coordination numbers. Attention has also been given to the forces network distributions, which

On the one hand, as perspective, through experiments and simulations, we believe that a more systematic study on the macroscopic roughness is needed to determine its impact on physical observables such as the packing fractions. On the other hand, theoretically, the focus should be on finding a way to approximate Edwards theory to our three scales. This would allow an easier characterization of particle shapes, possibly through coarse graining of the particle shapes. Moreover, focusing on other usual measure such as angle of repose of pile could help to support the idea our new roughnesses are indeed related to the usual coefficient of friction. Finally, it is obvious that these new findings on the meso-roughness can help to use less material when representing object for example through 3D printing but also help to reduce computational times in DEM as one can limit himself to a small number of spheres to get the right properties.

This work and further investigations thus help improve our understanding of granular matter and hence help industries take advantage of their properties.

Acknowledgements

A.L. research is supported by the ARC (Concerted Research Action) project EsPOIR (Eco-friendly

high Performance cOncrete for sustainable InfrastructuRes), funded by the Fédération Wallonie-Bruxelles. Computational resources have been provided by the Consortium des Équipements de Calcul Intensif (CÉCI), funded by the Fonds de la Recherche Scientifique de Belgique (F.R.S.-FNRS) under Grant No. 2.5020.11 and by the Walloon Region under the grant agreement n°1910247.

Author Contributions

A.L. performed the data analysis. A.L., E.O. developed the codes and wrote the manuscript. E.O. supervised the research.

Competing Interests

The authors declare no competing interests.

Data and Code availability

Code used to generate figures can be found in [62].

Appendix A Shape Characterization

Here we will show all the quantities needed to understand completely our different shapes (Rod, Cross and Star).

Let us first introduce how we describe these shapes via spheres, each of which is composed of rods with varying numbers of spheres. Two representatives are shown in Figure 1 with 3 and 32 spheres, our two extreme cases along with the length of a Rod L, the radius of a sphere R and the maximal furrow depth, which can be observed as f_3. In general, we place the spheres using,

$$r_{\text{coord}} = -\frac{L}{2} + 2i\left(\frac{L-2R}{2n-2}\right) + R \tag{A1}$$

where $L = 3R$ is the length of the rod, and n is the number of spheres chosen for the description $\{[3,12] \cup 32\}$. Here, i is associated with the index of the sphere ranging from 0 to $n-1$, and the subscript $_{\text{coord}}$ is just there to tell that you will choose a given coordinate along which the rod will tipically be placed along one, two or three Cartesian coordinates for the rod, cross and star, respectively. This formula ensures that the spheres will stay in $[-\frac{L}{2}, \frac{L}{2}]$, you then only need to check that there is not spheres placed multiple times at (0,0). Then, you can use a voxelization of those spheres to obtain the volume and moment of inertia occupied for each description by counting if cubes lies inside at least one sphere.

One could also ask how to obtain the limiting voxel and moment of inertia when $n \to \infty$. These values are related to the *Steinmetz solid* of two or three intersecting cylinders, denoted Stz2 and Stz3 hereafter. The idea is that one can easily compute the volume of cylinders and then only need to remove and add the correct overlaps. In this way,

$$\begin{aligned} \text{Rod} &= 1\ \text{Cylinder} + 1\ \text{Sphere} \\ \text{Cross} &= 2\ \text{Rod} - \text{Stz}_2 \\ \text{Star} &= 3\ \text{Rod} - \text{Stz}_2 + \text{Steinmetz}_3 \end{aligned} \tag{A2}$$

Note that Steinmetz_c denotes the intersection of c cylinders. Each volume and moment of inertia can be calculated analytically. We obtain for the volumes,

$$v_{\text{Rod}} = \frac{\pi}{3}(3\frac{L}{R} - 2)R^3 \tag{A3}$$

$$v_{\text{Stz2}} = \frac{16}{3}R^3 \tag{A4}$$

$$v_{\text{Stz3}} = 8(2-\sqrt{2})R^3 \tag{A5}$$

Using this approach, we can find the mass of each component via ρ. We then obtain for the moment of inertia of the rod along z,

$$I_{\text{Rod}-xx,yy} = \left(\frac{5\left(\frac{L}{R}\right)^3 - 10\left(\frac{L}{R}\right)^2 + 25\frac{L}{R} - 18}{60\frac{L}{R} - 40}\right) m_{\text{Rod}}R^2$$

$$I_{\text{Rod}-zz} = \left(\frac{15\frac{L}{R} - 14}{30\frac{L}{R} - 20}\right) m_{\text{Rod}}R^2$$

for an intersection of two cylinder along y and z,

$$I_{\text{Stz2}-xx} = \frac{8}{15}m_{\text{Stz2}}R^2$$

$$I_{\text{Stz2}-yy,zz} = \frac{7}{15}m_{\text{Stz2}}R^2$$

and finally, for three intersecting cylinder along the three Cartesian coordinates,

$$I_{\text{Stz3}-xx,yy,zz} = \frac{21-\sqrt{2}}{45} m_{\text{Stz3}} R^2$$

Our only remark here is to be careful about the orientation of the object when the composition rules presented in equation are used (A2).

The last quantities we must introduce are the furrow depth f_n and the volume of particles v_n with n spheres; we can see that both are linked. Let us first discuss what is furrow is; the furrow is the region between two spheres that might or might not overlap inside the description of our particles. In the case of a rod with 3 spheres, we thus have 2 furrows, two between each pair of spheres and in general there are $2(n-1)$ furrow for n overlapping spheres in a Rod. If one again assumes that our rod is along z, we can understand that the function associated with the depth of the furrow between two spheres, is thus that of a circle described by the coordinates (x_n, f_n, z_n). Moreover, we assume that one of the sphere is centred at (0,0,0). If we take a slice of our spheres with $x_n = 0$, the pair of circles always intersect at,

$$x_n = 0 \quad y_n = f_n = \pm\sqrt{R^2 - z_n^2} \quad z_n = \frac{2R}{n-1} \tag{A6}$$

Finally, the volume of the particles is found through one of the smooth particles, v_∞. Let us start with a rod, and we will generalize after, we have,

$$v_n = v_\infty - 2(n-1)v_{\text{furrow}}. \tag{A7}$$

since there is one furrow between each pair of spheres. If the rod is again along z, the volume of a furrow is then given simply by the integral,

$$\pi \int_0^{f_n} R^2 - z^2 dz = \frac{4\pi R^3}{3(n-1)^3} \tag{A8}$$

We thus have,

$$v_n = v_\infty - \frac{16\pi R^3}{3(n-1)^2} \tag{A9}$$

with equation (2) and (A2)–(A5), one can find that,

$$v_n = \frac{(1-\mu_{\text{meso}})^2 + 3}{4} v_\infty \tag{A10}$$

This equation summarizes the fact that a Rod with $\mu_{\text{meso}} = 0$ will have the volume of 3 spheres and the one with $\mu_{\text{meso}} = 1$, the one of 4 spheres and values in between connected by the meso scale roughness squared because it serves as a kind of radius in the computation of the volume of a furrow which has cylindrical symmetry. It can be extended to Cross and Star but some furrows will be filled inside the particles as $n \to \infty$ and will not truly change anything in the dynamic.

Appendix B Time-integration scheme

Given time step Δt, total time T, mass m, body inertia tensor $\mathbf{I}$ (in the body frame), state $\{\boldsymbol{r}, \boldsymbol{v}, \boldsymbol{q}, \boldsymbol{\omega}\}$, external/contact force $\boldsymbol{F}$ and torque $\boldsymbol{M}$ (computed from contacts), the cycle is as follows:

1. Initialization once at $t = 0$: set clump-sphere links and contact memory; pre-compute contacts; compute $\boldsymbol{F}^0$.
2. For $t = 0, \Delta t, \ldots, T - \Delta t$ do
   (a) Velocity update (explicit, translation + rotation):

$$\boldsymbol{v}^{n+\frac{1}{2}} = \boldsymbol{v}^n + \frac{\Delta t}{m} \boldsymbol{F}^n.$$

The angular quantities are transformed to the body frame with the current quaternion $\boldsymbol{q}^n$:

$$\boldsymbol{\omega}_b^n = \mathbf{R}(\boldsymbol{q}^n)^\top \boldsymbol{\omega}^n, \qquad \boldsymbol{M}_b{}^n = \mathbf{R}(\boldsymbol{q}^n)^\top \boldsymbol{M}^n,$$

and integrate Euler's rigid-body equation

$$\mathbf{I}\,\dot{\boldsymbol{\omega}}_b + \boldsymbol{\omega}_b \times (\mathbf{I}\,\boldsymbol{\omega}_b) = \boldsymbol{M}_b$$

with a 3-stage explicit RK scheme (coefficients as in your code):

$$\begin{aligned}
\boldsymbol{f}(\boldsymbol{w}, \boldsymbol{M}) &= \mathbf{I}^{-1}\big(\boldsymbol{M} - \boldsymbol{w} \times (\mathbf{I}\,\boldsymbol{w})\big), \\
\boldsymbol{k}_1 &= \Delta t\, \boldsymbol{f}(\boldsymbol{\omega}_b^n, \boldsymbol{M}_b{}^n), \\
\boldsymbol{w} &\leftarrow \boldsymbol{\omega}_b^n + \boldsymbol{k}_1, \\
\boldsymbol{k}_2 &= \Delta t\, \boldsymbol{f}(\boldsymbol{w}, \boldsymbol{M}_b{}^n), \\
\boldsymbol{w} &\leftarrow \boldsymbol{\omega}_b^n - \tfrac{3}{4}\boldsymbol{k}_1 + \tfrac{1}{4}\boldsymbol{k}_2, \\
\boldsymbol{k}_3 &= \Delta t\, \boldsymbol{f}(\boldsymbol{w}, \boldsymbol{M}_b{}^n), \\
\boldsymbol{\omega}_b^{n+\frac{1}{2}} &= \boldsymbol{\omega}_b^n + \tfrac{1}{6}\big(\boldsymbol{k}_1 + \boldsymbol{k}_2 + 4\boldsymbol{k}_3\big).
\end{aligned}$$

Return to the global frame:

$$\boldsymbol{\omega}^{n+\frac{1}{2}} = \mathbf{R}(\boldsymbol{q}^n)\,\boldsymbol{\omega}_b^{n+\frac{1}{2}}.$$

(b) Position and orientation update (quaternion rotation):

$$\boldsymbol{r}^{n+1} = \boldsymbol{r}^n + \boldsymbol{v}^{n+\frac{1}{2}}\,\Delta t.$$

Build the incremental rotation from the global angular velocity (angle–axis to unit quaternion):

$$\theta = \|\boldsymbol{\omega}^{n+\frac{1}{2}}\|\,\Delta t, \quad \boldsymbol{a} = \frac{\boldsymbol{\omega}^{n+\frac{1}{2}}}{\|\boldsymbol{\omega}^{n+\frac{1}{2}}\|},$$
$$\boldsymbol{p} = \big(\cos\tfrac{\theta}{2},\ \boldsymbol{a}\,\sin\tfrac{\theta}{2}\big),$$

then update and renormalize

$$\boldsymbol{q}^{n+1} = \boldsymbol{p} \otimes \boldsymbol{q}^n, \qquad \|\boldsymbol{q}^{n+1}\| = 1,$$

and rotate the body-frame basis (or subsequently use $\mathbf{R}(\boldsymbol{q}^{n+1})$):

$$\{\boldsymbol{e}_x, \boldsymbol{e}_y, \boldsymbol{e}_z\}^{n+1} = \mathbf{R}(\boldsymbol{p})\,\{\boldsymbol{e}_x, \boldsymbol{e}_y, \boldsymbol{e}_z\}^n.$$

Rebuild each sphere position from stored local offsets (x_i, y_i, z_i):

$$\boldsymbol{x}_i^{n+1} = \boldsymbol{r}^{n+1} + x_i\,\boldsymbol{e}_x^{n+1} + y_i\,\boldsymbol{e}_y^{n+1} + z_i\,\boldsymbol{e}_z^{n+1}.$$

(c) Contact preparation and force assembly at t^{n+1}: detect/update contacts; compute new $\boldsymbol{F}^{n+1}$ and $\boldsymbol{M}^{\,n+1}$ (external + contact).

(d) Velocity correction (explicit):

$$\boldsymbol{v}^{n+1} = \boldsymbol{v}^{n+\frac{1}{2}} + \frac{\Delta t}{m}\,\boldsymbol{F}^{n+1}.$$

Repeat step (b), the rotational RK step with $\boldsymbol{M}_b^{n+1}$ for a fully synchronized update.

Appendix C Clump–Clump Hertz–Mindlin Spring–Dashpot Contact

We consider a binary contact between two spherical surface elements attached to rigid clumps (indexed by $i = 1, 2$). Let R_i be the sphere radii, m_i the clump masses, $\mathbf{r}_{s_i}$ the sphere centers, $\mathbf{r}_{c_i}$ the clump centers, $\mathbf{v}_i$ the clump translational velocities, and $\boldsymbol{\omega}_i$ the clump angular velocities. The unit normal at the contact points from particle 1 to 2 is $\mathbf{n} \in \mathbb{R}^3$, and $\mathbf{t} \in \mathbb{R}^3$ is a unit tangent direction defined below. The normal overlap (penetration) is $\delta_n \geq 0$.

C.1 Effective quantities and contact stiffnesses

Define the effective radius and mass

$$R^* = \frac{R_1 R_2}{R_1 + R_2}, \qquad m^* = \frac{m_1 m_2}{m_1 + m_2}. \tag{C11}$$

Let E_i and ν_i be the Young's modulus and Poisson's ratio of material $i = 1, 2$, and let G_i be its shear modulus. Then E^* and G^* are the effective Young's and shear moduli of the contacting pair (material-dependent) and are defined, as follows:

$$E^* = \left[\frac{1-\nu_1^2}{E_1} + \frac{1-\nu_2^2}{E_2}\right]^{-1}, \qquad G^* = \left[\frac{1-\nu_1}{G_1} + \frac{1-\nu_2}{G_2}\right]^{-1}. \tag{C12}$$

The Hertz–Mindlin normal and tangential stiffness prefactors are

$$K_n = \frac{4}{3}\,E^*\sqrt{R^*}, \qquad K_t = 8\,G^*\sqrt{R^*}. \tag{C13}$$

With the current normal overlap δ_n, the incremental (secant) stiffnesses used at each step are

$$k_n = K_n\sqrt{\delta_n}, \qquad k_t = K_t\sqrt{\delta_n}. \tag{C14}$$

C.2 Kinematics and relative velocity at the contact point

The contact points on each clump are offset from the clump centres by the lever arms

$$\boldsymbol{\ell}_1 = \mathbf{r}_{s_1} - \mathbf{r}_{c_1} - R_1\mathbf{n}, \qquad \boldsymbol{\ell}_2 = \mathbf{r}_{s_2} - \mathbf{r}_{c_2} + R_2\mathbf{n}. \tag{C15}$$

The rotational contribution to the relative velocity at the contact is

$$\mathbf{v}_r = \boldsymbol{\omega}_2 \times \boldsymbol{\ell}_2 - \boldsymbol{\omega}_1 \times \boldsymbol{\ell}_1, \tag{C16}$$

and the total relative velocity is

$$\mathbf{v} = (\mathbf{v}_2 - \mathbf{v}_1) + \mathbf{v}_r. \tag{C17}$$

Its normal and tangential components are as follows:

$$v_n \;=\; \mathbf{v}\cdot\mathbf{n}, \qquad \mathbf{v}_t \;=\; \mathbf{v} - v_n\mathbf{n}. \tag{C18}$$

Tangential slip history

Let $\mathbf{s}$ be the accumulated tangential displacement (a history variable) and $\delta_t = \|\mathbf{s}\|$ its magnitude. With time step Δt, the update is

$$\mathbf{s} \leftarrow \mathbf{s} + \mathbf{v}\,\Delta t, \quad \mathbf{s} \leftarrow \mathbf{s} - \big(\mathbf{s}\cdot\mathbf{n}\big)\mathbf{n}, \quad \delta_t \leftarrow \|\mathbf{s}\|, \tag{C19}$$

$$\text{if } \delta_t > 0: \quad \mathbf{t} \leftarrow \mathbf{s}/\delta_t, \quad v_t \leftarrow \mathbf{v}\cdot\mathbf{t}; \tag{C20}$$

otherwise set $\mathbf{t}$ arbitrarily in the tangent plane and $v_t = 0$.

C.3 Damping from coefficient of restitution

Given a normal coefficient of restitution $e \in (0, 1)$, define

$$\beta \;=\; \frac{\pi}{\ln(e)}, \qquad \alpha \;=\; \frac{5}{6}, \tag{C21}$$

$$\gamma \;=\; \sqrt{\frac{4\alpha}{1+\beta^2}}, \qquad \phi \;=\; \gamma\sqrt{m^*}. \tag{C22}$$

The normal and tangential dashpot coefficients used at the current step are then

$$\eta_n \;=\; \phi\,\sqrt{k_n}, \qquad \eta_t \;=\; \phi\,\sqrt{k_t}. \tag{C23}$$

C.4 Contact forces with Coulomb friction

The trial (pre yield) normal and tangential forces are as follows,

$$F_n^{\mathrm{tr}} \;=\; k_n\,\delta_n + \eta_n\,v_n, \qquad F_t^{\mathrm{tr}} \;=\; k_t\,\delta_t + \eta_t\,v_t, \tag{C24}$$

with non adhesive normal contact

$$F_n \;=\; \max\big(0,\, F_n^{\mathrm{tr}}\big). \tag{C25}$$

Let μ be the (Coulomb) friction coefficient. The stick/slip condition is enforced by

$$\text{If } k_t\delta_t \le \mu F_n \;\;(\text{stick}): \quad F_t \;=\; F_t^{\mathrm{tr}}, \tag{C26}$$

$$\text{Else (slip)}: \quad F_t \;=\; \mu F_n, \quad \delta_t \leftarrow \frac{F_t}{k_t}, \quad \mathbf{s} \leftarrow \delta_t\,\mathbf{t}. \tag{C27}$$

The contact force vector is

$$\mathbf{F} \;=\; F_n\mathbf{n} + F_t\mathbf{t}. \tag{C28}$$

C.5 Action–reaction and contact torques

The equal-and-opposite contact forces are applied to the clumps,

$$\mathbf{F}_1 \;=\; \mathbf{F}, \qquad \mathbf{F}_2 \;=\; -\mathbf{F}. \tag{C29}$$

The contact torques (about the clump centres) are

$$\boldsymbol{\tau}_1 \;=\; \boldsymbol{\ell}_1 \times \mathbf{F}, \qquad \boldsymbol{\tau}_2 \;=\; \boldsymbol{\ell}_2 \times (-\mathbf{F}). \tag{C30}$$

C.6 Algorithmic summary per time step

Given $(\delta_n, \mathbf{n})$ at time t, the state $(\mathbf{s}, \delta_t, \mathbf{t})$, and kinematics $(\mathbf{r}_{s_i}, \mathbf{r}_{c_i}, \mathbf{v}_i, \boldsymbol{\omega}_i)$:

1. Compute $\boldsymbol{\ell}_i$ $\mathbf{v}_r$, and $\mathbf{v}$ via respectively (C15), (C16) and (C17).
2. Update $\mathbf{s}$, δ_t, $\mathbf{t}$, v_n, v_t via (C18)–(C20).
3. Form k_n, k_t via (C14) and η_n, η_t via (C23).
4. Compute F_n and F_t via (C24)–(C27).
5. Apply $\mathbf{F}$, $\boldsymbol{\tau}_1$, $\boldsymbol{\tau}_2$ via (C28)–(C30).

Notes

(i) The tangential history $\mathbf{s}$ is stored in the global (inertial) frame and re-projected each step to remain in the contact plane, consistent with (C20). (ii) The restitution-to-damping mapping (C22) matches the implementation here and may differ from alternative DEM calibrations. (iii) No rolling resistance or adhesion is included.

Appendix D Forces distributions

In Figure D1, we present a representative distribution of tangent and normal forces for the rod. Note that the forces F are usually normalized with the mean force $\bar{F}$ observed in the pile so that all the forces lie on a master curve with behaviour proportional to $A\exp\left(-\beta\tilde{F}\right)$ for $\tilde{F} > 1$ [56–58]. We then report the fitting parameters A and β in Figure D2. We did not observe a significant change with the meso-roughness but did observer a significant change with with the macro-roughness.

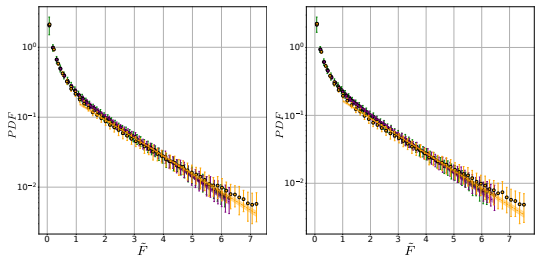


Fig. D1 Probability distribution of the mean observed forces $\tilde{F}$ along the normal and tangential directions of the contacts.

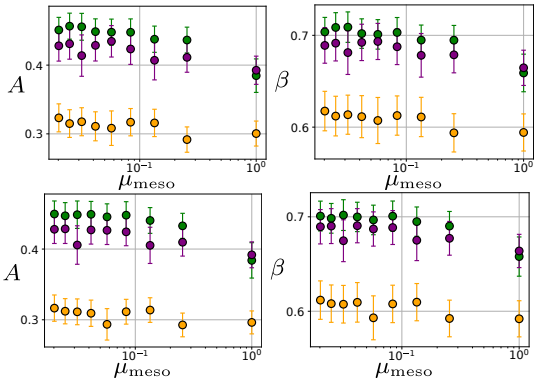


Fig. D2 Amplitude and decay rates of the exponential fit for the mean observed normal and tangential forces $\tilde{F} > 1$.

References

[1] Weaire, D., Aste, T.: The Pursuit of Perfect Packing, 2nd edn. CRC Press, Boca Raton (2008). https://doi.org/10.1201/9781420068184

[2] Lu, G., Third, J.R., Müller, C.R.: Discrete element models for non-spherical particle systems: From theoretical developments to applications. Chemical Engineering Science **127**, 425–465 (2015) https://doi.org/10.1016/j.ces.2014.11.050 . Accessed 2025-09-22

[3] Scherer, V., Wirtz, S., Krause, B., Wissing, F.: Simulation of Reacting Moving Granular Material in Furnaces and Boilers An Overview on the Capabilities Of the Discrete Element Method. Energy Procedia **120**, 41–61 (2017) https://doi.org/10.1016/j.egypro.2017.07.154 . Accessed 2025-09-22

[4] Zhao, J., Zhao, S., Luding, S.: The role of particle shape in computational modelling of granular matter. Nat Rev Phys **5**(9), 505–525 (2023) https://doi.org/10.1038/s42254-023-00617-9 . Publisher: Nature Publishing Group. Accessed 2025-10-21

[5] Thilakarathna, P.S.M., Kristombu Baduge, K.S., Mendis, P., Vimonsatit, V., Lee, H.: Mesoscale modelling of concrete – A review of geometry generation, placing algorithms, constitutive relations and applications. Engineering Fracture Mechanics **231**, 106974 (2020) https://doi.org/10.1016/j.engfracmech.2020.106974 . Accessed 2025-09-22

[6] Rukeyser, M.: The Traces of Thomas Hariot. Random House, New York (1971)

[7] Hales, T., Adams, M., Bauer, G., Dang, T.D., Harrison, J., Hoang, L.T., Kaliszyk, C., Magron, V., Mclaughlin, S., Nguyen, T.T., Nguyen, Q.T., Nipkow, T., Obua, S., Pleso, J., Rute, J., Solovyev, A., Ta, T.H.A., Tran, N.T., Trieu, T.D., Urban, J., Vu, K., Zumkeller, R.: A FORMAL PROOF OF THE KEPLER CONJECTURE. Forum of Mathematics, Pi **5**, 2 (2017) https://doi.org/10.1017/fmp.2017.1 . Accessed 2025-10-28

[8] Borkovec, M., De Paris, W., Peikert, R.: The fractal dimension of the apollonian sphere packing. Fractals **02**(04), 521–526 (1994) https://doi.org/10.1142/S0218348X94000739 . Publisher: World Scientific Publishing Co. Accessed 2025-10-28

[9] Furnas, C.C.: Grading Aggregates - I. - Mathematical Relations for Beds of Broken Solids of Maximum Density. Archive Location: world Publisher: American Chemical Society (2002). https://doi.org/10.1021/ie50261a017 . https://pubs.acs.org/doi/pdf/10.1021/ie50261a017 Accessed 2025-10-28

[10] Farr, R.S., Groot, R.D.: Close packing density of polydisperse hard spheres. J. Chem. Phys. **131**(24), 244104 (2009) https://doi.org/10.1063/1.3276799 . Accessed 2025-10-28

[11] Baule, A., Morone, F., Herrmann, H.J.,

Makse, H.A.: Edwards statistical mechanics for jammed granular matter. Rev. Mod. Phys. **90**(1), 015006 (2018) https://doi.org/10.1103/RevModPhys.90.015006 . Publisher: American Physical Society. Accessed 2025-09-22

[12] Edwards, S.F., Oakeshott, R.B.S.: Theory of powders. Physica A: Statistical Mechanics and its Applications **157**(3), 1080–1090 (1989) https://doi.org/10.1016/0378-4371(89)90034-4 . Accessed 2025-09-22

[13] Torquato, S.: Perspective: Basic understanding of condensed phases of matter via packing models. J. Chem. Phys. **149**(2), 020901 (2018) https://doi.org/10.1063/1.5036657 . Accessed 2025-09-22

[14] Blouwolff, J., Fraden, S.: The coordination number of granular cylinders. EPL **76**(6), 1095 (2006) https://doi.org/10.1209/epl/i2006-10376-1 . Publisher: IOP Publishing. Accessed 2025-09-22

[15] Gravish, N., I. Goldman, D.: Entangled Granular Media. In: Fluids, Colloids and Soft Materials, pp. 341–354. John Wiley & Sons, Ltd, Hoboken, NJ (2016). https://doi.org/10.1002/9781119220510.ch17

[16] Graaf, J., Roij, R., Dijkstra, M.: Dense Regular Packings of Irregular Nonconvex Particles. Phys. Rev. Lett. **107**(15), 155501 (2011) https://doi.org/10.1103/PhysRevLett.107.155501 . Publisher: American Physical Society. Accessed 2025-09-22

[17] Benítez-Zamudio, J.E., Hidalgo-Caballero, S., Pacheco-Vázquez, F.: Penetration of Rigid Rods, Flexible Rods, and Granular Jets into Low-Density Granular Media. arXiv (2026). https://doi.org/10.48550/ARXIV.2603.27262 . https://arxiv.org/abs/2603.27262

[18] Aponte, D., Barés, J., Renouf, M., Azéma, E., Estrada, N.: Experimental exploration of geometric cohesion and solid fraction in columns of highly non-convex Platonic polypods. Granular Matter **27**(1), 27 (2025) https://doi.org/10.1007/s10035-024-01490-8 . Accessed 2025-09-22

[19] Ringlein, J., Robbins, M.O.: Understanding and illustrating the atomic origins of friction. Am. J. Phys. **72**(7), 884–891 (2004) https://doi.org/10.1119/1.1715107 . Accessed 2025-10-27

[20] Blau, P.J.: The significance and use of the friction coefficient. Tribology International **34**(9), 585–591 (2001) https://doi.org/10.1016/S0301-679X(01)00050-0 . Accessed 2025-10-27

[21] He, G., Müser, M.H., Robbins, M.O.: Adsorbed Layers and the Origin of Static Friction. Science **284**(5420), 1650–1652 (1999) https://doi.org/10.1126/science.284.5420.1650 . Publisher: American Association for the Advancement of Science. Accessed 2025-10-27

[22] Menezes, P.L., Kishore, Kailas, S.V.: Influence of roughness parameters on coefficient of friction under lubricated conditions. Sadhana **33**(3), 181–190 (2008) https://doi.org/10.1007/s12046-008-0011-8 . Accessed 2025-10-27

[23] Urbakh, M., Klafter, J., Gourdon, D., Israelachvili, J.: The nonlinear nature of friction. Nature **430**(6999), 525–528 (2004) https://doi.org/10.1038/nature02750 . Publisher: Nature Publishing Group. Accessed 2025-10-27

[24] Silbert, L.E.: Jamming of frictional spheres and random loose packing. Soft Matter **6**(13), 2918 (2010) https://doi.org/10.1039/c001973a

[25] Farrell, G.R., Martini, K.M., Menon, N.: Loose packings of frictional spheres. Soft Matter **6**(13), 2925 (2010) https://doi.org/10.1039/c0sm00038h

[26] Fukumoto, Y., Sakaguchi, H., Murakami, A.: The role of rolling friction in granular packing. Granular Matter **15**(2), 175–182 (2013) https://doi.org/10.1007/s10035-013-0398-8 . Accessed 2025-09-22

[27] Liu, W., Jin, Y., Chen, S., Makse, H.A., Li, S.: Equation of state for random sphere packings with arbitrary adhesion and friction. Soft Matter **13**(2), 421–427 (2017) https://doi.org/10.1039/c6sm02216b

[28] Yang, S., Zhou, W., Liu, J., Qi, T., Ma, G.: Role of Inter-particle Friction in Granular Materials Under Three Dimensional Conditions. CIMNE, Barcelona (2019). Pages: 388-399. https://hdl.handle.net/2117/186605 Accessed 2025-09-22

[29] Santos, A.P., Bolintineanu, D.S., Grest, G.S., Lechman, J.B., Plimpton, S.J., Srivastava, I., Silbert, L.E.: Granular packings with sliding, rolling, and twisting friction. Phys. Rev. E **102**(3), 032903 (2020) https://doi.org/10.1103/PhysRevE.102.032903 . Publisher: American Physical Society. Accessed 2025-09-22

[30] Liang, J., Feng, X., Zheng, N., Wang, H., Ni, R., Zhang, Z.: Glass Transition in Monolayers of Rough Colloidal Ellipsoids. Phys. Rev. Lett. **134**(3), 038202 (2025) https://doi.org/10.1103/PhysRevLett.134.038202 . Publisher: American Physical Society. Accessed 2025-09-22

[31] Pol, A., Artoni, R., Richard, P.: Unified scaling law for wall friction in laterally confined flows of shape anisotropic particles. Physical Review Fluids **8**(8) (2023) https://doi.org/10.1103/physrevfluids.8.084302

[32] Iwashita, K., Oda, M.: Micro-deformation mechanism of shear banding process based on modified distinct element method. Powder Technology **109**(1), 192–205 (2000) https://doi.org/10.1016/S0032-5910(99)00236-3 . Accessed 2025-10-21

[33] Ai, J., Chen, J.-F., Rotter, J.M., Ooi, J.Y.: Assessment of rolling resistance models in discrete element simulations. Powder Technology **206**(3), 269–282 (2011) https://doi.org/10.1016/j.powtec.2010.09.030 . Accessed 2025-10-21

[34] Wensrich, C.M., Katterfeld, A.: Rolling friction as a technique for modelling particle shape in DEM. Powder Technology **217**, 409–417 (2012) https://doi.org/10.1016/j.powtec.2011.10.057 . Accessed 2025-10-21

[35] Estrada, N., Azéma, E., Radjai, F., Taboada, A.: Identification of rolling resistance as a shape parameter in sheared granular media. Phys. Rev. E **84**(1), 011306 (2011) https://doi.org/10.1103/PhysRevE.84.011306 . Publisher: American Physical Society. Accessed 2025-10-23

[36] Zhou, L., Chu, X., Xu, Y.: DEM investigation on characteristics of rolling resistance for modelling particle shape. EPJ Web Conf. **140**, 05005 (2017) https://doi.org/10.1051/epjconf/201714005005 . Publisher: EDP Sciences. Accessed 2025-10-23

[37] Behringer, R.P., Chakraborty, B.: The physics of jamming for granular materials: a review. Reports on Progress in Physics **82**(1), 012601 (2018) https://doi.org/10.1088/1361-6633/aadc3c

[38] Preud'homme, N., Schockmel, J., Opsomer, E., Lumay, G.: Tribocharging of granular materials flowing in grounded inclined tubes. Soft Matter **20**(45), 9060–9067 (2024) https://doi.org/10.1039/d4sm01082e

[39] Favier, J.F., Abbaspour-Fard, M.H., Kremmer, M., Raji, A.O.: Shape representation of axi-symmetrical, non-spherical particles in discrete element simulation using multi-element model particles. Engineering Computations **16**(4), 467–480 (1999) https://doi.org/10.1108/02644409910271894 . Accessed 2025-09-22

[40] Jia, X., Williams, R.A.: 3D-measurement of particles and particulate assemblies - A review of the paradigm shift in describing anisotropic particles. Powder Technology **447**, 120109 (2024) https://doi.org/10.1016/j.powtec.2024.120109 . Accessed 2025-09-22

[41] Bićanić, N.: Discrete Element Methods. In: Encyclopedia of Computational Mechanics. John Wiley & Sons, Ltd, Chichester, UK (2007). https://doi.org/10.1002/0470091355.ecm006.pub2

[42] Ulusoy, U.: A Review of Particle Shape Effects on Material Properties for Various Engineering Applications: From Macro to Nanoscale. Minerals **13**(1), 91 (2023) https://doi.org/10.3390/min13010091 . Publisher: Multidisciplinary Digital Publishing Institute. Accessed 2025-09-22

[43] Dosta, M., Andre, D., Angelidakis, V., Caulk, R.A., Celigueta, M.A., Chareyre, B., Dietiker, J.-F., Girardot, J., Govender, N., Hubert, C., Kobyłka, R., Moura, A.F., Skorych, V., Weatherley, D.K., Weinhart, T.: Comparing open-source DEM frameworks for simulations of common bulk processes. Computer Physics Communications **296**, 109066 (2024) https://doi.org/10.1016/j.cpc.2023.109066 . Accessed 2025-09-22

[44] Cundall, P.A., Strack, O.D.L.: A discrete numerical model for granular assemblies. Geotechnique **29**(1), 47–65 (1979) https://doi.org/10.1680/geot.1979.29.1.47 . Accessed 2025-09-22

[45] Kuipers, J.B.: Quaternions and Rotation Sequences: A Primer with Applications to Orbits, Aerospace, and Virtual Reality. Princeton University Press, Princeton, NJ (1999). https://doi.org/10.1515/9780691211701

[46] Valle, C.A., Angelidakis, V., Roy, S., Muñoz, J.D., Pöschel, T.: SPIRAL: An efficient algorithm for the integration of the equation of rotational motion. Computer Physics Communications **297**, 109077 (2024) https://doi.org/10.1016/j.cpc.2023.109077 . Accessed 2025-09-22

[47] Bufolo, G.N., Sobral, Y.D.: Analysis of the leapfrog-Verlet method applied to the Kuwabara-Kono force model in discrete element method simulations of granular materials. Adv Comput Math **50**(4), 82 (2024) https://doi.org/10.1007/s10444-024-10162-3 . Accessed 2025-09-22

[48] Hairer, E., Lubich, C., Wanner, G.: Geometric numerical integration illustrated by the Störmer–Verlet method. Acta Numerica **12**, 399–450 (2003) https://doi.org/10.1017/S0962492902000144 . Accessed 2025-09-22

[49] Feng, Y.T.: Thirty years of developments in contact modelling of non-spherical particles in DEM: a selective review. Acta Mech. Sin. **39**(1), 722343 (2023) https://doi.org/10.1007/s10409-022-22343-x . Accessed 2025-09-22

[50] Janssen, H.A.: Versuche über getreidedruck in silozellen. Zeitschr. d. Vereines deutscher Ingenieure **39**, 1045–1049 (1895)

[51] Sperl, M.: Experiments on corn pressure in silo cells – translation and comment of janssen's paper from 1895. Granular Matter **8**(2), 59–65 (2005) https://doi.org/10.1007/s10035-005-0224-z

[52] Windows-Yule, C.R.K., Mühlbauer, S., Cisneros, L.A.T., Nair, P., Marzulli, V., Pöschel, T.: Janssen effect in dynamic particulate systems. Physical Review E **100**(2) (2019) https://doi.org/10.1103/physreve.100.022902

[53] Lu, G., Hidalgo, R.C., Third, J.R., Müller, C.R.: Ordering and stress transmission in packings of straight and curved spherocylinders. Granular Matter **18**(3) (2016) https://doi.org/10.1007/s10035-016-0637-x

[54] Freeman, J.O., Peterson, S., Cao, C., Wang, Y., Franklin, S.V., Weeks, E.R.: Random packing of rods in small containers. Granular Matter **21**(4), 84 (2019) https://doi.org/10.1007/s10035-019-0939-x . Accessed 2026-01-16

[55] Jaoshvili, A., Esakia, A., Porrati, M., Chaikin, P.M.: Experiments on the Random Packing of Tetrahedral Dice. Phys. Rev. Lett. **104**(18), 185501 (2010) https://doi.org/10.1103/PhysRevLett.104.185501 . Accessed 2026-01-16

[56] Radjai, F., Jean, M., Moreau, J.-J., Roux, S.: Force Distributions in Dense Two-Dimensional Granular Systems. Phys. Rev. Lett. **77**(2), 274–277 (1996) https://doi.org/10.1103/PhysRevLett.77.274 . Publisher:

American Physical Society. Accessed 2025-09-25

[57] Mueth, D.M., Jaeger, H.M., Nagel, S.R.: Force distribution in a granular medium. Phys. Rev. E **57**(3), 3164–3169 (1998) https://doi.org/10.1103/PhysRevE.57.3164 . Publisher: American Physical Society. Accessed 2025-09-25

[58] Danylenko, V.A., Mykulyak, S.V., Polyakovskyi, V.O., Kulich, V.V., Oleynik, I.I.: Force distribution in a granular medium under dynamic loading. Phys. Rev. E **96**(1), 012906 (2017) https://doi.org/10.1103/PhysRevE.96.012906 . Publisher: American Physical Society. Accessed 2025-09-25

[59] Erikson, J.M., Mueggenburg, N.W., Jaeger, H.M., Nagel, S.R.: Force distributions in three-dimensional compressible granular packs. Phys. Rev. E **66**(4), 040301 (2002) https://doi.org/10.1103/PhysRevE.66.040301 . Publisher: American Physical Society. Accessed 2025-10-24

[60] Azéma, E., Radjaï, F.: Force chains and contact network topology in sheared packings of elongated particles. Physical Review E **85**(3) (2012) https://doi.org/10.1103/physreve.85.031303

[61] Conzelmann, N.A., Penn, A., Partl, M.N., Clemens, F.J., Poulikakos, L.D., Müller, C.R.: Link between packing morphology and the distribution of contact forces and stresses in packings of highly nonconvex particles. Physical Review E **102**(6) (2020) https://doi.org/10.1103/physreve.102.062902

[62] Luyckx, A., Opsomer: Mesocopic-Roughness. Zenodo (2026). https://doi.org/10.5281/zenodo.19455025 . https://github.com/GRASP-LAB/Mesocopic-Roughness